THE JOURNAL OF PHYSICAL CHEMISTRY A
A JOURNAL OF THE AMERICAN CHEMICAL SOCIETY

pubs.acs.org/JPCA

Article

Infrared Spectroscopic Studies of Oxygen Atom Quantum Diffusion in Solid Parahydrogen

Ibrahim Muddasser, Anh H. M. Nguyen, Aaron I. Strom, Aaron M. Hardee, Bryan G. Pluid, and David T. Anderson*

Cite This: *J. Phys. Chem. A* 2023, 127, 2751−2764

Read Online

ACCESS | Metrics & More | Article Recommendations | Supporting Information

ABSTRACT: The thermally induced diffusion of atomic species in noble gas matrices was studied extensively in the 1990s to investigate low-temperature solid-state reactions and to synthesize reactive intermediates. In contrast, much less is known about the diffusion of atomic species in quantum solids such as solid parahydrogen (p-H_2). While hydrogen atoms were shown to diffuse in normal-hydrogen solids at 4.2 K as early as 1989, the diffusion of other atomic species in solid p-H_2 has not been reported in the literature. The *in situ* photogeneration of atomic oxygen, by ArF laser irradiation of an O_2-doped p-H_2 solid at 193 nm, is studied here to investigate the diffusion of O(^3P) atoms in a quantum solid. The O(^3P) atom mobility is detected by measuring the kinetics of the O(^3P) + O_2 → O_3 reaction after photolysis via infrared spectroscopy of the O_3 reaction product. This reaction is barrierless and is thus assumed to be diffusion-controlled under these conditions such that the reaction rate constant can be used to estimate the oxygen atom diffusion coefficient. The O_3 growth curves are well fit by single exponential expressions allowing the pseudo-first-order rate constant for the O(^3P) + O_2 → O_3 reaction to be extracted. The reaction rates are affected strongly by the p-H_2 crystal morphology and display a non-Arrhenius-type temperature dependence consistent with quantum diffusion of the O(^3P) atom. The experimental results are compared to H(^2S) atom reaction studies in p-H_2, analogous studies in noble gas matrices, and laboratory studies of atomic diffusion in astronomical ices and surfaces.

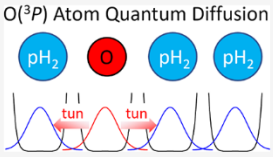

1. INTRODUCTION

Over the past several decades, solid parahydrogen (p-H_2) has developed into a viable host for a variety of matrix isolation studies, especially in applications that take advantage of the quantum mechanical properties of cryogenic solid hydrogen.[1−9] By comparison, noble gases have been more extensively utilized as matrix isolation hosts and for much longer (more than 60 years).[10−15] However, except for helium and, to some extent, neon, these matrix hosts form classical van der Waals solids. Solid p-H_2 is a quantum solid,[16−19] which is distinguished from classical solids in that the zero-point kinetic energy of a single p-H_2 molecule in the crystal lattice is comparable to its potential energy, and the root-mean-square displacement of a p-H_2 molecule from its lattice site is a significant fraction (∼18%) of the nearest-neighbor spacing.[18] In this way, quantum hosts provide new opportunities for studying condensed phase photophysics and chemistry that could not be explored using classical noble gas matrices. For example, p-H_2 is particularly advantageous when used as a host for *in situ* guest molecule photochemical studies because the cage effect in solid p-H_2 is minimal,[2] and photolysis can be used to directly produce isolated photofragments. In contrast, the *in situ* photochemistry in solid argon or even solid neon is typically dominated by caging of the nascent photofragments by the matrix host.[11] Thus, the outcome of an *in situ* photochemistry experiment of the same guest species in solid argon and in solid p-H_2 can be qualitatively different, and therefore, noble gas and p-H_2 matrix hosts can be used for different purposes and to complement each other.

Yet, as the name matrix isolation implies, one of the important issues is how well does the matrix localize (isolate) the guest species and prevent it from diffusing through the matrix and reacting with itself or other species. Accordingly, the diffusion of atomic guest species in noble gas crystals has been extensively studied and, for the most part, is well characterized experimentally for H, O, and F atoms in the various noble gas matrices.[11,20] Much less is known about the diffusion of classical and quantum impurities in a quantum host. For example, while hydrogen atom diffusion in solid normal-H_2 (n-H_2) was first observed more than 50 years ago using ESR spectroscopy,[21] there still are many unanswered questions about the details of H atom quantum diffusion in solid p-H_2. In terms of more classical guest species like an oxygen atom, even less is known. Further complicating our understanding of guest diffusion in solid p-H_2 is that both HF[22] and H_2O[23] have been reported to quantum-diffuse in solid p-H_2. This was unexpected, and there still is no definitive explanation of how the HF and H_2O molecules diffuse through

Received: January 12, 2023
Revised: March 2, 2023
Published: March 17, 2023

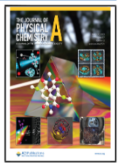

the p-H_2 matrix host. The objective in this study is to determine if oxygen atoms diffuse in solid p-H_2 and if they do, what does the diffusion rate depend upon, i.e., crystal morphology, temperature, and guest concentration.

One photochemical system that we have been interested in for a long time is the 193 nm photochemistry of molecular oxygen in solid p-H_2. Photodissociation of molecular oxygen at 193 nm produces two O atoms in their ground electronic state $O(^3P)$; the 193 nm photon energy is not capable of producing $O(^1D)$.[24] Therefore, early on, we recognized that the *in situ* 193 nm photolysis of O_2 in solid p-H_2 should produce $O(^3P)$ atoms that cannot react with the p-H_2 host even by quantum mechanical tunneling because the $O(^3P) + H_2 \rightarrow OH + H$ reaction is slightly endothermic (ΔH = +970 cm^{-1}).[25] However, when we conducted O_2 photolysis experiments at 193 nm, we observed rapid production of H_2O and, at longer times after the photolysis laser is turned off, growth in HOO and O_3 side products was observed. We now believe that the production of H_2O can be traced to the production of O_3 early in the photolysis exposure, which in turn gets photodissociated by the 193 nm radiation to produce O_2 and $O(^1D)$.[26] It is $O(^1D)$ that can react with the p-H_2 host to create H_2O and H atoms. We therefore used the 193 nm *in situ* photolysis of $^{17}O_2$ to create both ortho-$H_2{}^{17}O$ and para-$H_2{}^{17}O$ to study the nuclear spin conversion of water in solid p-H_2.[27] We also have shown that the 193 nm photolysis of formic acid in solid p-H_2 produces H_2O satellite peaks that we believe to be the result of reactions of $O(^1D)$ and/or OH with the p-H_2 host that ultimately produce H_2O next to a vacancy in solid p-H_2.[28,29] In the current O_2 photolysis studies in solid p-H_2, we purposely altered the 193 nm photolysis conditions to minimize the production of $O(^1D)$ so that we could try to produce $O(^3P)$-doped solid p-H_2.

The mobility of atomic species on solid surfaces is an important factor in our understanding of the low-temperature chemistry that occurs in and on the icy coatings of dust grains in interstellar space.[30,31] If species such as O atoms freeze out and become immobilized on the surface of grains, then the chemistry can be dominated by mobile H atoms, and the chemical evolution of the grain would be very different than if O atoms can diffuse on the surface (or into the bulk). Experiment[32−34] and atomistic simulations[35−37] have shown that H and O atoms can diffuse on amorphous water surfaces down to low temperatures (∼10 K) and this can lead to the formation of diatomic or larger molecules (O_2, O_3, and CO_2) in the laboratory experiments.[32−34] Given the long processing times that are available in translucent, diffuse, and dense molecular clouds,[30,31] these types of surface reactions may play a significant role in the chemical processes occurring in interstellar space. However, whether the O atom diffuses by quantum tunneling or by thermal hopping is still controversial[38] and an unresolved problem. Reaction studies in solid p-H_2 therefore offer model systems for the study of ice chemistry where pronounced quantum effects in the host allow for the quantum diffusion of guest atoms in the bulk so that the kinetics of solid-state chemical reactions can be probed in the laboratory. The photochemical studies of O_2 photolysis in solid p-H_2 presented here therefore can be compared with experimental studies conducted in noble gas matrices, on amorphous silicates, and on solid amorphous water that are motivated by astrochemical measurements. Comparison of the studies in solid p-H_2 to the investigations motivated by astrochemistry can therefore show similarities and differences that can be used to better understand the low-temperature ice chemistry.

2. MATERIALS AND METHODS

The p-H_2 matrix isolation apparatus used in this investigation has been described previously.[27] We employ the rapid vapor deposition (RVD) technique[39,40] developed by Fajardo and Tam to grow O_2-doped p-H_2 crystals on a BaF_2 optical substrate held at ∼2.5 K during deposition within a sample-in-vacuum liquid He bath cryostat. A Si-diode mounted to the bottom of the substrate holder (T_B) is used for temperature measurements. The vacuum shroud is evacuated with a turbomolecular pump to below 10^{-6} torr at room temperature. In these experiments, 99.97% p-H_2-enriched solids are prepared on the fly by passing normal-H_2 gas through a home-built ortho/para converter operated near 14 K during deposition. The concentration of O_2 in the p-H_2 solid is controlled by varying the dopant flow rate with respect to the p-H_2 flow rate, which is set to a constant value of 308(16) mmol/h for this set of experiments. The average film thickness is 0.14(2) cm, samples are grown in 20 min, and a thin pure p-H_2 layer is deposited before and after the co-deposition to ensure that the O_2 is well isolated.

Molecular oxygen is photolyzed at 193 nm using the output of an ArF excimer laser (GAM Laser EX5). The ArF laser beam impinges on the crystal at 45° with respect to the substrate surface normal and is aligned to overlap with the FTIR beam. The laser fluence is measured with a power meter after the laser beam passes through an iris just before the CaF_2 photolysis window of the cryostat. In these studies, we varied the photolysis conditions by changing the repetition rate of the laser (25 to 250 Hz) and the duration (15 s to 10 min) of the 193 nm exposure.

High-resolution IR spectra are recorded using an FTIR spectrometer (Bruker IFS-120/5-HR) with the IR beam focused through the cryostat and recollimated with off-axis parabolic mirrors (8″ effective focal length) in a transmission optical setup. Two different FTIR setups were employed in this work: (1) IR spectra from 1800 to 8000 cm^{-1} at 0.03 cm^{-1} resolution were recorded using a tungsten source, KBr beam splitter, and InSb detector and (2) spectra from 650 to 3900 cm^{-1} at 0.02 cm^{-1} resolution are measured using a globar source, KBr beam splitter, and MCT detector. During and after photolysis, while studying the photoinduced kinetics, a long pass filter is used to block IR radiation above 3900 cm^{-1} from the FTIR source from impinging on the sample to minimize any possible effects of near-IR light on the photoinduced kinetics. For the kinetic measurements, we define the end of the 193 nm photolysis as time zero and use the midpoint in time for each FTIR scan (start time + scan time/2) for each data point. To record the reaction kinetics with sufficient time resolution, the first ∼100 min of the reaction kinetics is measured with 210 s FTIR scan times (res = 0.03 cm^{-1}, 16 averages) and then with 315 s scan times (24 averages) thereafter. This allows us to record the kinetics with the best tradeoff between signal-to-noise and time resolution.

We report spectroscopically determined dopant concentrations in parts per million (ppm) using the following equation,

$$[C] = \frac{\ln(10) V_0}{\varepsilon_c l} \int A_{10}(\tilde{\nu}) d\tilde{\nu} \ (1 \times 10^6) \quad (1)$$

https://doi.org/10.1021/acs.jpca.3c00266
J. Phys. Chem. A 2023, 127, 2751−2764

where C is the species of interest, $A_{10}(\tilde{\nu})$ is the decadic absorbance as a function of wavenumber, ε_c is the integrated absorption coefficient for the transition used, l is the IR pathlength through the crystal determined from the integrated intensity of the $Q_1(0) + S_0(0)$ and $S_1(0) + S_0(0)$ double transitions of solid p-H_2,[41] and V_0 is the molar volume of solid p-H_2 at liquid helium temperatures (23.16 cm^3 mol^{-1}).[18] The integrated absorption coefficients and integration limits used in this work are reported in Table S1 in the Supporting Information. To measure the O_2 concentration, the same apparatus was also used to carry out control measurements on the complete photolysis of an O_2-doped p-H_2 sample where the sample was photolyzed for 216 min at 71(5) mW/cm^2 to convert all O_2 to H_2O (and small concentrations of HOO and O_3) to correlate the O_2 flow rate to the O_2 concentration in the p-H_2 solid. By using a constant p-H_2 flow rate in all the depositions, we can control the O_2 concentration by adjusting the O_2 flow rate. More details on how the O_2 concentrations reported in this work are measured are reported in the Supporting Information.

To investigate how the crystallinity of the chemically doped p-H_2 sample influences the photoinduced kinetics, we studied as-deposited and annealed samples. The term "as-deposited" refers to p-H_2 samples right after deposition,[39] which have not been exposed to sample temperatures above ∼2.5 K. As documented in numerous studies,[6,40,42−47] the RVD method produces polycrystalline as-deposited p-H_2 solids that contain metastable face-centered-cubic (fcc) and hexagonal-close-packed (hcp) crystal structures. Warming the sample to 4.0 K for several minutes irreversibly anneals the solid to a nearly pure hcp crystal structure and results in a high degree of alignment of the c-axis of the hcp crystallites with the substrate surface normal.[43,44] This annealing process is quantified[46−48] in this study by measuring the fraction of hcp crystal structures, $X_{hcp} = N_{hcp}/(N_{hcp} + N_{fcc})$, using the zero phonon $U_0(0)$ solid p-H_2 single transition near 1167.1 cm^{-1}. Only p-H_2 molecules in hcp crystal sites that lack a center of inversion can contribute to the integrated intensity of the $U_0(0)$ transition such that the integrated intensity can be used to monitor X_{hcp} using the following equation,

$$X_{hcp} = 2.303 \frac{cV_0}{\tilde{\alpha} l \tilde{\nu}_0 N_A} \int A_{10}(\tilde{\nu}) d\tilde{\nu} \quad (2)$$

where c is the speed of light *in vacuo*, $\alpha\sim$ is the $U_0(0)$ absorption coefficient (51.0(2.5) × 10^{-17} cm^3 s^{-1} molecule^{-1}),[49] N_A is Avogadro's constant, and $\nu\sim_0$ is the peak frequency of the transition in cm^{-1}. Consequently, X_{hcp} should have values between 0 and 1 and can be used to quantify the crystallinity of the sample.

3. RESULTS

3.1. Infrared Spectroscopy of O_3 Trapped in Solid p-H_2. In general, the infrared absorption bands of a guest molecule isolated in a matrix host are inhomogeneously broadened by the distribution of solvation sites occupied by the dopant.[50] Accordingly, the line shape reflects how homogeneous a particular matrix site is for a guest species, and sometimes, multiple peaks are observed when multiple trapping sites are populated. The spectra recorded at different times during an O_2/p-H_2 photolysis experiment are shown in Figure 1 in the region of the ν_3 (antisymmetric stretch) vibrational fundamental of ozone. This band is easily assigned

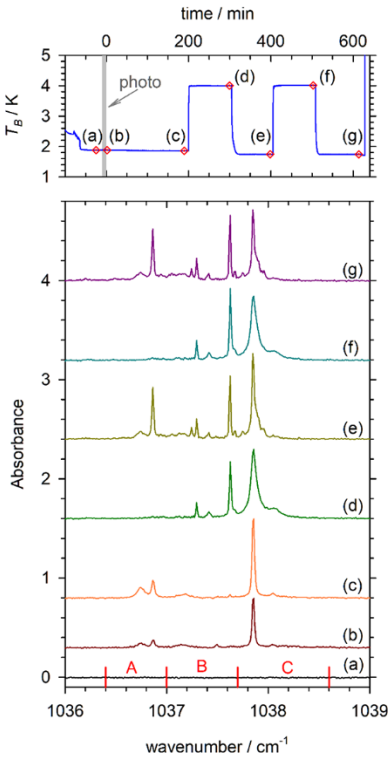

Figure 1. Infrared spectra in the region of the ν_3 fundamental for an O_2/p-H_2 matrix sample (L04). (Top) Sample temperature (T_B) recorded at 1 Hz during a 193 nm photolysis experiment. The gray bar indicates the timing and duration of the photolysis exposure. The red diamonds labeled with letters indicate the time and temperature when a spectrum in the bottom series of spectra was recorded. (Bottom) Series of infrared spectra recorded at different times labeled with letters on the temperature trace. Note that we divide the ν_3 band into three regions labeled *A*, *B*, and *C*, respectively, where the integration limits are shown on the wavenumber axis. See the text for more details.

to $^{16}O_3$ based on comparison with the ν_3 peak frequencies reported for $^{16}O_3$ in noble gas matrices.[51] The top graph shows the T_B temperature log recorded at 1 Hz during the experiment, and the gray bar represents the time and duration of a 193 nm photolysis exposure. The different red diamonds labeled with letters on the temperature trace indicate the temperature and time when a spectrum in the bottom series of spectra was recorded. For example, trace (a) in Figure 1 was recorded at 1.88 K before photolysis and no ozone absorptions are observed in this region, as expected. The ν_3 vibrational mode is the most intense O_3 band we can observe with our FTIR setup, and we will use the ν_3 band to measure the O_3 concentration. Trace (b) was recorded only 1.91 min after photolysis and showed the ozone spectrum recorded for an as-deposited p-H_2 sample. There are multiple peaks measured in trace (b), and therefore, we divided the ν_3 spectrum into three integration regions labeled *A*, *B*, and *C* and showed the integration limits at the bottom of Figure 1 (more details are presented in Table S1 in the Supporting Information). The most prominent peak in the as-deposited spectrum is at 1037.85 cm^{-1} with a 0.03 cm^{-1} FWHM, but there are small peaks in the *A* integration region as well. Trace (c) was recorded approximately 187.3 min after trace (b) while maintaining the sample at 1.86(1) K, and it clearly shows that all the O_3 peaks grow in intensity presumably due to O

https://doi.org/10.1021/acs.jpca.3c00266
J. Phys. Chem. A 2023, 127, 2751−2764

atom diffusion and reaction with O_2. Trace (d) shows the spectrum recorded after raising the temperature to 4.0 K for approximately 100 min. The peaks in region *A* completely disappear at 4.0 K, and the strong absorption in region *C* broadens significantly while new peaks appear in region *B*. The first time the temperature of the as-deposited sample is raised above ∼3.5 K, the sample anneals, and irreversible changes occur in the ozone ν_3 spectrum. These irreversible changes are thought to be due to changes in the polycrystalline host matrix, which converts from fcc to hcp upon annealing and tends to align the *c*-axis of the hcp crystallites parallel to the substrate surface normal.[6,40,42−47] Therefore, by comparing trace (d) with trace (c), we observe the combined effects of annealing and increased temperature on the ν_3 spectrum. To disentangle the reversible and irreversible effects of temperature, we must temperature-cycle the sample after annealing.

As discussed in the previous paragraph, we observe irreversible changes in the ν_3 spectrum of O_3 when the sample is annealed. We also observe reversible changes with temperature, which signal changes in the population of O_3 in different matrix sites with temperature. For example, traces (d) and (f) recorded at 4 K are very similar, and traces (e) and (g) recorded at 1.7 K are also remarkably similar. After annealing, the peak positions remain constant, but the intensity of the different features changes with temperature. The two peaks in region (*A*) increase in intensity at low temperature but almost completely go away in the spectra recorded at 4 K. Furthermore, the total integrated intensity of the ν_3 band remains relatively constant (not shown in Figure 1) with changes in temperature, but the relative intensities of the various peaks change. We will show that the total integrated intensity of the ν_3 band remains constant when we discuss the kinetics of O_3 growth in the next section. The changes in intensity displayed in Figure 1 with temperature suggest that ozone populates at least two distinct matrix sites in the p-H_2 matrix and that the populations of these different matrix sites change with temperature over the 1.7 to 4.0 K temperature range.

It is informative to compare the ν_3 spectrum of O_3 trapped in a p-H_2 matrix with the spectra recorded for O_3 trapped in noble gas matrices. First, two features were repeatedly observed in the ν_3 region for O_3 trapped in neon, argon, krypton, and xenon.[51] The energy difference between the two ν_3 absorptions ranged from 0.94 to 1.65 cm^{-1} for the different noble gas hosts, and the vibrational frequencies of both features decrease from argon to xenon as expected; they decrease (matrix shifts to lower energy) with the increased attractive intermolecular interactions of O_3 with the more polarizable noble gas matrices. Interestingly, the ν_3 peaks observed in neon do not fit this trend appearing at lower wavenumbers than argon.[51] The two ν_3 features in argon, krypton, and xenon show reversible changes with temperature; the higher wavenumber feature broadens more rapidly with an increase in temperature in argon than the lower wavenumber feature.[51] Computer simulations of the infrared spectrum of O_3 trapped in noble gas matrices assigned both features to the O_3 monomer with the higher and lower energy peaks assigned to double and single substitution sites, respectively.[52]

The ν_3 spectrum of ozone in solid p-H_2 has many similarities with the noble gas matrix isolation spectra. The separation between the major peaks in regions (*A*) and (*C*) is 0.99 cm^{-1}, which is within the range observed for noble gas matrices. The lower wavenumber peak in region (*A*) decreases in intensity with an increase in temperature, like what is observed in the noble gas matrices for the higher wavenumber peak. Nonetheless, the O_3 absorption features in solid p-H_2 are narrower and there are more resolved peaks in comparison with the O_3 spectra recorded in noble gas matrices. This too is expected since p-H_2 is a quantum solid and the increased amount of zero-point energy allows for a more homogeneous matrix site where small defects can be annealed away by zero-point energy or tunneling. However, there can still be multiple trapping sites populated by a dopant because even when zero-point motion is considered, O_3 trapped in one matrix site can be at a slightly different energy than O_3 trapped in a different matrix site. If this energy difference is small with respect to the available thermal energy, then two sites can be populated simultaneously. Thus, multiple trapping sites are possible in a quantum solid, but the total energy (potential energy plus zero-point energy) is what matters, not just the potential energy.

In addition to the ozone ν_3 features observed around 1040 cm^{-1}, we also observe the $\nu_1 + \nu_3$ combination band at 2105.8 cm^{-1}. We monitor the para-H_2O concentration using the $1_{11} \leftarrow 0_{00}$ rovibrational transition built off of the ν_2 bending mode that occurs at 1631.6 cm^{-1} and the HOO concentration using the ν_2 band at 1100 cm^{-1}. See Table S1 in the Supporting Information for more details. We note that all three HOO fundamentals are observed in this study, but we use the ν_2 band with the greatest absorption strength to measure the HOO concentration. We chose to use the ν_2 absorption to monitor the para-H_2O concentration because the $1_{11} \leftarrow 0_{00}$ rovibrational peak can be optimally measured with the same FTIR setup used to monitor the ν_3 absorption of O_3. Last, Tahsildaran *et al.* reported a large discrepancy (up to a factor of 2) between the H_2O concentrations measured using the corresponding rovibrational peaks in the ν_2 and ν_3 regions, even though the gas phase line intensities are well established.[53] Using the integration protocols listed in Table S1 in the Supporting Information, we did not observe the same large discrepancies in the para-H_2O concentration; we analyzed the para-H_2O concentrations determined using the ν_2 and ν_3 vibrational modes in all the experiments presented here and found that the ratio of concentrations determined using $\nu_2/\nu_3 = 0.96 \pm 0.12$. Thus, we feel confident in the para-H_2O concentrations reported here but also believe that the discrepancies identified by Tahsildaran *et al.* warrant further study (see the Supporting Information for more details).[53]

3.2. O_3 Growth Kinetics. We can separate the O_3 growth kinetics into three separate categories based upon the reaction conditions: low-temperature as-deposited, low-temperature annealed, and high-temperature annealed. We will start by discussing the O_3 growth kinetics for low-temperature as-deposited O_2-doped p-H_2 crystals. A typical ozone kinetic trace for a low-temperature as-deposited sample is shown in Figure 2. The gray vertical bar in Figure 2 represents the timing and duration of the 193 nm photolysis exposure. This sample was photolyzed for 10 min at 25 Hz with a fluence of 14(2) mW/cm^2, and the initial O_2 concentration was 421(5) ppm. For the experiment shown in Figure 2, the average X_{hcp} value during the reaction kinetics is $X_{hcp} = 0.609(9)$, which is typical of an as-deposited p-H_2 sample. As soon as the photolysis starts, we observe rapid growth in the O_3 concentration, presumably due to photoinduced $O(^3P)$ atom mobility. The bond energy[54] of the ground electronic state of O_2 is 5.115 eV, and thus, there is 1.299 eV of excess energy available to the two $O(^3P)$ atom

https://doi.org/10.1021/acs.jpca.3c00266
J. Phys. Chem. A 2023, 127, 2751−2764

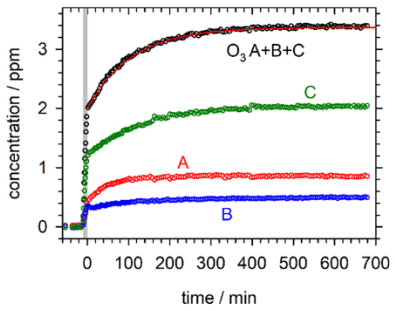

Figure 2. Ozone growth kinetics for an as-deposited O_2/p-H_2 sample (L01, X_{hcp} = 0.609(9)) recorded at 1.85(1) K. The total O_3 concentration is plotted as black circles, and the effective concentration is determined from the three integration regions labeled *A*, *B*, and *C*, respectively. The red line is the result of a least-squares fit of the data to eq 3. See the text for more details.

fragments from the 193 nm photolysis (E_{photon} = 6.414 eV). Upon 193 nm photolysis, therefore, the $O(^3P)$ atoms exit the p-H_2 solvation cage and migrate through the p-H_2 solid until they thermally equilibrate. The unfavorable kinematics for the O + H_2 → OH + H reaction indicates that only 11.19% of the available energy is in the center-of-mass collision frame so that almost no reaction of the nascent O atom with the p-H_2 host is expected under these photolysis conditions. Note that we plot the effective O_3 concentration determined from integrating regions *A*, *B*, and *C* as described earlier along with the total O_3 concentration in Figure 2. After the ArF laser is shut off, the O_3 concentration continues to increase for up to 600 min (10 h). It is difficult to believe that this growth represents reactions of electronically excited O_2 or O atoms because these excited states should relax in the millisecond time frame.[55] Instead, we assert that the continued growth of O_3 after photolysis is due to quantum diffusion of the $O(^3P)$ atoms that diffuse through the p-H_2 matrix until they encounter an intact O_2 molecule and then react without a barrier to form O_3. The solid p-H_2 matrix rapidly dissipates the excess energy deposited in the O_3 reaction product, and the nascent O_3 molecules equilibrate to the bulk p-H_2 temperature.

We can fit the data after photolysis to the following analytical expression for single exponential growth,

$$[O_3]_t = [O_3]_0 + A(1 - \exp(-k't)) \quad (3)$$

where $[O_3]_0$ is the concentration of ozone at time t = 0 (immediately after photolysis), A is the magnitude of the O_3 concentration growth after photolysis, k' is the first-order rate constant, and t is defined as the time after photolysis. The solid red line in Figure 2 is the result of a least-squares fit of the data to eq 3. As can be seen in Figure 2, the data fit very well to this first-order expression, which is qualitatively different from the thermally induced O atom reaction kinetics measured in noble gas matrices.[50] The O_3 growth curves generated from integrating the three different ν_3 regions show that after photolysis, O_3 is produced in matrix sites with peaks located primarily in the *C* and *A* regions, whereas peaks in the *B* region increase much less. This indicates that the reaction preferentially makes O_3 in certain matrix sites, and during reaction, there can also be conversion from one matrix site to another; otherwise, all three growth curves (*A*, *B*, and *C*) should have the same shape. We will discuss this further in the next section.

The photolysis conditions are set to ensure pseudo-first-order reaction kinetics ($[O_2] \gg [O(^3P)]$), whereby we estimate based on the 193 nm absorption cross section for O_2 ($\sigma = 10^{-21}$ cm^2)[55] that a 10 min photolysis with a fluence of 14(2) mW/cm^2 will decrease the O_2 concentration from 421 to 418 ppm and produce 6−7 ppm of $O(^3P)$ atoms. We also want to keep the $O(^3P)$ atom concentration low to minimize the possibility of O atom recombination ($O(^3P) + O(^3P) \rightarrow O_2$). Note that we use the UV absorption cross section measured for O_2 trapped in noble gas solids, which is approximately three orders of magnitude larger than in gas phase O_2 due to matrix-induced mixing of the excited electronic states accessed at 193 nm.[56] Given that the $O(^3P) + O_2 \rightarrow O_3$ reaction is barrierless,[57,58] the slowest step in the reaction mechanism is likely the diffusion of the reactants to adjacent lattice sites. We therefore expect to measure first-order O_3 growth kinetics where the extracted rate constant is proportional to the $O(^3P)$ atom diffusion coefficient. We also use short 193 nm photolysis exposures to minimize the amount of O_3 that gets photodissociated to produce $O(^1D)$ atoms. As we will show, by doing this, we keep the generation of H atoms at a minimum so that we can study the $O(^3P) + O_2 \rightarrow O_3$ reaction in isolation. In total, we conducted five photolysis experiments on as-deposited, low-temperature O_2/p-H_2 samples. The kinetic parameters determined from the fits are presented in Table S3, and all the kinetic plots for these experiments are presented in Figures S3−S7 in the Supporting Information.

3.3. Crystal Morphology. One would expect that if the $O(^3P)$ atom migrated via quantum diffusion, then the rate constant for the $O(^3P) + O_2 \rightarrow O_3$ reaction should not depend strongly on temperature but rather may depend on the p-H_2 crystal structure. Specifically, quantum diffusion of an impurity in solid p-H_2 is typically the fastest in crystals that have very few defects and are homogeneous, i.e., single crystals with long-range order.[19,59−65] Quantum diffusion of an impurity via tunneling between two adjacent lattice sites is the most facile when the solvation energy of the guest species in the two sites is degenerate. Thus, as-deposited samples, which are polycrystalline and contain mixed fcc/hcp crystal domains with most likely other defects as well (vacancies, stacking faults, grain boundaries, etc.), should show slower $O(^3P)$ atom quantum diffusion rates where an $O(^3P)$ atom can get pinned near a defect or tunnels more slowly through the p-H_2 matrix. In Figure 3, we show the full O_3 kinetic trace for the experiment depicted in Figure 1, which is a photolysis experiment conducted on an as-deposited sample but where, after the reaction has occurred for about 200 min, we quickly ramped the temperature of the sample to 4.0 K. What we observe is that while the reaction kinetics were slowing down at the 200 min mark in the as-deposited sample presumably because the $O(^3P)$ atom concentration is decreasing as the $O(^3P)$ atoms react, by raising the temperature, we see another burst of O_3 growth. Note that the changes shown in Figure 3 after the temperature is raised to 4.0 K are not caused by an increased sublimation rate at the higher temperature; we have verified that at 4.0 K, for samples this thick (see Table S2 in the Supporting Information), we cannot detect a change in the thickness even while holding the sample at 4.0 K for almost 10 h. However, once the sample had been annealed at 4.0 K for about 100 min, we cooled the sample back down to 1.75(1) K and kept recording the kinetics. We then quickly raised the temperature for a second time and observed no further growth

https://doi.org/10.1021/acs.jpca.3c00266
J. Phys. Chem. A 2023, 127, 2751−2764

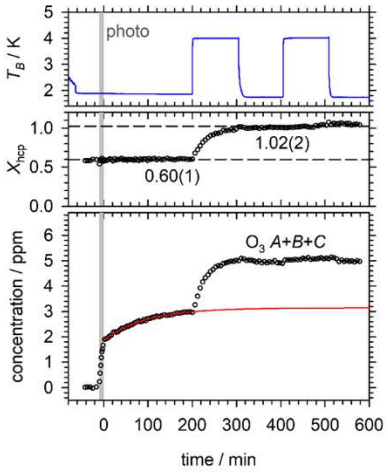

Figure 3. Measured ozone growth kinetics for a low-temperature, as-deposited O_2/p-H_2 sample (L04) showing the effects of raising the temperature during the reaction. The reaction kinetics were measured for the first 200 min after photolysis and fit to eq 3, and the red line is the fitted curve. At 200 min, the temperature of the sample quickly increased to 4.05(2) K for approximately 100 min. When the sample is first annealed, the O_3 concentration increases rapidly. Subsequent changes in temperature have little effect on the O_3 concentration. See the text for further details.

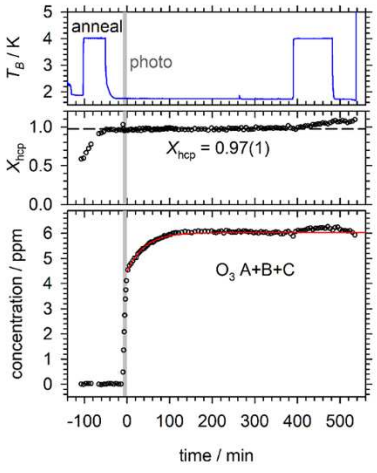

Figure 4. The measured ozone growth kinetics for an annealed O_2/p-H_2 sample (A02) showed the effects of raising the temperature during the reaction. The reaction kinetics were measured for the first 390 min after photolysis and fit to eq 3, and the red line is the fitted curve. At the 390 min mark, the temperature of the sample was quickly increased to 4.00(1) K for approximately 100 min. For the annealed sample, raising the temperature produces no new O_3 growth in contrast to the results for the as-deposited sample.

in the O_3 concentration. We interpret this experiment as follows: the first time we raised the temperature (T_B > 3.5 K), we annealed the as-deposited sample as evidenced by the sharp rise in the X_{hcp} value (see Figure 3 around the 200 min mark). The X_{hcp} value starts at X_{hcp} = 0.60(1) in the as-deposited sample and quickly rises to X_{hcp} = 1.02(2) after raising the temperature of the sample to 4.0 K. We believe that some of the $O(^3P)$ atoms produced in the 193 nm photolysis of the as-deposited sample get pinned near defects and are immobilized. By annealing the crystal, we produce mesoscopic changes in the p-H_2 crystal structure and, during this annealing process, $O(^3P)$ atoms are mobilized and move through the p-H_2 solid. The second time we raised the temperature around the 400 min mark, however, we observe no change in the O_3 concentration. That is, increasing the temperature alone does not produce the increase in O_3 growth, rather, it is the irreversible physical changes in the p-H_2 crystal structure produced by annealing that cause the release of more $O(^3P)$ atoms.

To check our interpretation of the experiment shown in Figure 3, we performed the analogous experiment on a low-temperature annealed sample where we anneal the sample prior to photolysis. The results of this experiment are shown in Figure 4 where an O_2-doped p-H_2 sample was annealed at 4.0 K prior to the 193 nm photolysis. After annealing, the sample had an X_{hcp} = 0.97(1), indicating that the sample was annealed. Under identical photolysis conditions as the as-deposited sample displayed in Figure 3, we photolyze the sample and then, after the laser is shut off, measure the subsequent O_3 reaction kinetics for about 400 min. This time, when we raise the temperature, we observe no new burst of O_3 growth. That is, for the annealed sample, increasing the temperature did not produce any more O_3. Interestingly, the comparison of the two experiments in Figures 3 and 4 shows that the annealed sample produced a higher yield of O_3, but comparable amounts of O_3 were produced only after the as-deposited sample was annealed. To summarize, the p-H_2 crystal morphology has a large effect on the reaction kinetics, showing that the yield of O_3 molecules is less for as-deposited samples because all the $O(^3P)$ atoms that are produced are not mobile and some are trapped at defect sites. Annealing the as-deposited sample after photolysis can be used to release most of these $O(^3P)$ atoms to permit further reactions. We now must quantitatively measure the O + O_2 reaction kinetics for low-temperature annealed samples to see if the rate constant for the O_3 growth increases as expected for quantum diffusion.

We therefore performed six experiments on the low-temperature reaction kinetics for annealed O_2-doped p-H_2 samples. The answer to the question of do the reaction kinetics speed up in annealed samples is partially revealed in Figure 4 where we observe faster O_3 growth kinetics for the first 400 min of the annealed sample before we raise the temperature. We performed four experiments in addition to the experiment shown in Figure 4 on annealed samples for the full duration of the hold time of the helium cryostat. Representative kinetic plots of the low-temperature annealed experiments are shown in Figures S8−S13, and the fitted parameters are displayed in Table S3, both in the Supporting Information. As we will show in the following section, the rate constant extracted from annealed samples is more than two times greater than the rate constant extracted from as-deposited samples.

3.4. Effect of Temperature. After we determined that the reaction kinetics are faster in annealed samples compared to as-deposited samples, we wanted to measure the effect of temperature. For this, we can compare the rate constants extracted from annealed samples at both low and high temperatures. In this way, we disentangle the effects of temperature and crystal morphology on the rate constant because we only compare annealed samples for the effect of temperature. We performed several experiments at 4.0 K and found that the O + O_2 reaction is more difficult to characterize at this higher temperature. The main reason is that when the photolysis is carried out at 4.0 K, it produces more mobile H atoms that can interfere with the O + O_2 reaction kinetics.

https://doi.org/10.1021/acs.jpca.3c00266
J. Phys. Chem. A 2023, 127, 2751−2764

However, if we photolyze the sample at high repetition rates for short amounts of time, where we do not detect significant production of para-H_2O during photolysis or high HOO concentrations after photolysis, we can measure the O + O_2 reaction kinetics at 4.0 K. We conducted seven photolysis experiments at high temperature ($T_B \geq 4.0$ K); one experiment (H02) conducted at 4.45(3) K failed because the O_3 concentration decreased after photolysis, instead of increasing like expected, due presumably to competing reactions with H atoms. For the remaining six high-temperature experiments, H01 produced ~26 ppm of HOO and H04 suffered from a small O_3 growth after photolysis, which makes it hard to precisely determine the rate constant (k'). Nonetheless, four of the 4.0 K experiments where the production of H atoms was kept minimal gave reproducible data, and we report all the fitted parameters in Table S3 and show the corresponding kinetics plots in Figures S14−S21 in the Supporting Information.

The kinetic experiments at 4.0 K also produced the greatest variation in the fitted rate constant. If we use all six measurements, we determine an average rate constant k' = 0.031 ± 0.012 min^{-1}. However, if we remove the two outliers (H01 and H04), then we determine k' = 0.0244 ± 0.0045 min^{-1}, which is comparable to the rate constant determined for the annealed samples at low temperature. We believe that this is the best determination of k' at 4.0 K where perturbations due to H atoms are kept at a minimum. So, as might be expected for quantum diffusion-controlled reaction kinetics, increasing the temperature from 1.7 to 4.0 K did not increase the rate constant significantly. The O_2-doped p-H_2 samples that are studied at 4.0 K typically reach higher X_{hcp} values than the analogous experiments at lower temperatures just because the sample takes longer to anneal. We plot the extracted pseudo-first-order rate constants (k') as a function of X_{hcp} for the three types of samples in Figure 5. The four rate constants

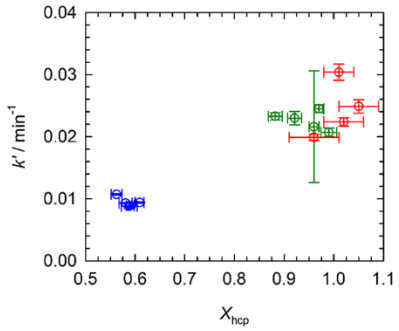

Figure 5. Plot of the measured pseudo-first-order rate constants (k') for O_3 growth versus X_{hcp}. The low-temperature as-deposited, low-temperature annealed, and high-temperature annealed samples are plotted as blue circles, green circles, and red circles, respectively. The error bars represent the uncertainties from the fit (one standard deviation) and statistical errors in X_{hcp}. Note that the smallest rate constants are measured for as-deposited p-H_2 samples.

extracted for as-deposited samples (blue circles) show a tight grouping at around X_{hcp} = 0.6 in Figure 5 and the smallest rate constants of all three categories of the sample. The annealed samples (green circles) have significantly larger rate constants than the as-deposited samples, and there is greater spread in the X_{hcp} values. The four rate constants measured for annealed samples (red circles) at 4.0 K are comparable to the rate constants determined for the low-temperature annealed samples. As shown in Figure 5, the difference between the high- and low-temperature annealed samples is subtle, there is greater variation in the extracted rate constant for the high temperature data, and the high temperature data typically have higher X_{hcp} values, but the rate constants measured at 1.7 and 4.0 K are comparable. This is further proof that the O(^3P) atoms are quantum-diffusing and that thermal energy is not required to make the O(^3P) atom hop from lattice site to lattice site (non-Arrhenius behavior). Thus, these reaction kinetics are under very different diffusion conditions than the analogous bimolecular reactions performed in noble gas solids where the diffusion is thermally activated.

4. DISCUSSION

4.1. Comparison with H Atom Diffusion Studies in Solid p-H_2. Now that we have established that O(^3P) atoms quantum-diffuse in solid p-H_2, it is interesting to compare the measured kinetics with analogous studies of H(^2S) atom reaction kinetics in solid p-H_2. To do so, we first convert the pseudo-first-order rate constants measured here ($k' = k[O_2]_0$) to second-order rate constants in standard units using the initial O_2 concentration. Assuming that the reaction to form O_3 is diffusion-controlled, we can also derive the O(^3P) atom diffusion coefficient from the second-order rate constant

$$k = 4\pi r_0 D \tag{4}$$

where r_0 is the separation for reactive capture, and D is the mutual diffusion coefficient for the reacting species (O + O_2). We took $r_0 \approx 3.79$ Å, the nearest-neighbor spacing in solid p-H_2, which assumes that when an O(^3P) atom and O_2 molecule become nearest neighbors, a reaction always occurs to produce O_3. We present these results in Table 1 along with the rate constants and diffusion coefficients measured for H atom recombination in solid n-H_2 and solid p-H_2, respectively.[21,66]

The second-order rate constants and diffusion coefficients measured for the three categories of samples in this work show that crystal morphology has the dominant effect in diffusion-controlled O(^3P) atom reactions in solid p-H_2. As discussed earlier, the rate constant more than doubles from going from as-deposited to annealed samples. In contrast, raising the temperature from 1.7 to 4.0 K has a much lesser effect on the reaction rate constant as expected for O(^3P) atom quantum diffusion. In these studies, we also performed one O + O_2 reaction kinetic experiment where we only exposed the sample to IR radiation when we took the spectra every hour. Based on this control experiment (A05), mid-IR irradiation (650−3900 cm^{-1}) of the sample by the FTIR source caused no measurable effect on the reaction kinetics. In addition, all spectral measurements were performed with a long pass filter (<3861 cm^{-1}) in the FTIR beam path such that no near-IR radiation impinged on the sample during kinetic measurements. We originally thought that near-IR excitation of the p-H_2 solid could cause the O(^3P) atoms to react with $H_2(v = 1)$ in analogy to our findings for Cl atoms in solid p-H_2.[67,68] However, while we did not study this in detail in this study, we believe that near-IR light also does not significantly influence the O(^3P) atom reaction kinetics.

The fact that the O(^3P) atom diffusion coefficients measured here are comparable to the literature values for the H atom is unexpected for a variety of reasons: (i) it is known[65] that H atoms quantum-diffuse through p-H_2 by repeated H + H_2 → H_2 + H chemical reactions, while this mechanism is not possible for O(^3P) atoms, (ii) the O atom has a mass that is 16

https://doi.org/10.1021/acs.jpca.3c00266
J. Phys. Chem. A 2023, 127, 2751−2764

Table 1. Measured Average Rate Constants and Diffusion Coefficients for Atoms in Cryogenic Solids

species	k (cm^3 mol^{-1} s^{-1})	D (cm^2 s^{-1})	temperature (K)	matrix	ref.
O, as-deposited	9.3(10)	$3.2(3) \times 10^{-17}$	1.8	p-H_2	this work
O, annealed	21.8(7)	$7.6(2) \times 10^{-17}$	1.7	p-H_2	this work
O, annealed	23(5)	$8.1(17) \times 10^{-17}$	4.0	p-H_2	this work
H, annealed	81.7(82)	$2.7(3) \times 10^{-16}$	4.2	n-H_2	21
H, annealed	50(5)	$1.7(2) \times 10^{-16}$	4.2	p-H_2	66
H, recomb.	0.08(2)	$3.2(4) \times 10^{-19}$	0.67	n-H_2	69
H, spatial diff		$1.5(1) \times 10^{-16}$	0.67	n-H_2	69
H, recomb.	0.9(8)	$1(1) \times 10^{-18}$	0.67	p-H_2	69
H, spatial diff		$4(1) \times 10^{-17}$	0.67	p-H_2	69

times greater than a H atom and, thus, O atom tunneling should be roughly 4 times less probable, and (iii) the rate of quantum diffusion should be inversely proportional to the guest concentration.[48] While we did not test the effect of the O_2 concentration on the measured kinetics thoroughly in this study, the one experiment (L02) on an as-deposited sample with an initial O_2 concentration of 157(3) ppm gave a rate constant k = 22.0(9) cm^3 mol^{-1} s^{-1} compared to the average rate constant for the four other as-deposited samples (k = 9.3(10) cm^3 mol^{-1} s^{-1}) with an average initial O_2 concentration of 399(16) ppm. This finding of a greater second-order rate constant at lower O_2 concentrations is consistent with our picture of $O(^3P)$ atom quantum diffusion, namely, that greater O_2 concentrations disrupt the long-range translational order of the p-H_2 crystal and tend to slow down the quantum-diffusing particle.[48] Thus, in this study, the average initial O_2 concentration is approximately 403(18) ppm compared to the previous measurements on H atom recombination in n-H_2 ($[H]_0$ = 1.2 and 3.0 ppm)[21] and p-H_2 ($[H]_0$ = 3.0 ppm).[66] Therefore, one would expect that the $O(^3P)$ atom diffusion rates could be even larger if the O + O_2 reaction kinetics could be performed at lower initial O_2 concentrations.

We can also compare the O atom diffusion rates measured here with more recent measurements of H atom diffusion in n-H_2 and p-H_2 thin films. The previous measurements[21,66] of the diffusion coefficient for H atoms in solid n-H_2 and p-H_2, respectively, were based on measuring the kinetics of H atom recombination. Measuring the diffusion coefficient indirectly this way may introduce systematic errors due to the nature of quantum diffusion. When the distance between the recombining H atoms is small, the major potential inhomogeneity for quantum tunneling is associated with the interaction of the pairing particles.[66] This can cause the final stages of recombination to be very slow, or to not occur at all, because the tunneling bandwidth is much smaller than the energy level mismatch caused by the interacting particles. This possibility was pointed out in the paper that measured the H atom diffusion coefficient where they observed an "absence" of recombination in heavily enriched p-H_2 solids.[66] However, in more recent measurements in H_2 thin films at temperatures below 1 K, the H atom recombination kinetics can be distinguished from spatial diffusion driven by a concentration gradient, allowing these researchers to test for this systematic bias.[69,70] As shown in Table 1, these researchers showed that for both n-H_2 and p-H_2 thin films, the H atom diffusion coefficient measured for pure spatial diffusion is one to two orders of magnitude larger than the diffusion coefficient obtained from H atom recombination. This is consistent with our picture of quantum diffusion where the diffusion is the fastest when the atom propagates through a periodic matrix potential via resonant tunneling. Thus, the diffusion coefficient measured from the reaction kinetics provides a lower limit to the actual H atom diffusion coefficient because it necessarily includes the final stages of recombination where the tunneling diffusion potentially slows down significantly. Note also that these more recent measurements show larger variations in the extracted diffusion coefficients and rate constants for the p-H_2 thin films. This again is consistent with the H atom recombination kinetics depending strongly on the o-H_2 content in the sample as first shown by Kumada *et al.*,[66] and in enriched p-H_2 solids, the H atom recombination rate depends sensitively on the other experimental conditions (crystal morphology, H atom concentration, and phonons) as well.

To compare the quantum diffusion of $O(^3P)$ atoms with $H(^2S)$ atoms at a more quantitative level, we approximate the quantum diffusion of a guest species as repeated tunneling events through square barrier potentials. We can estimate the time constant for tunneling through a single square barrier using the following expression,

$$k(s^{-1}) = \nu_0 \exp\left[-\frac{2a}{\hbar}\sqrt{2mE_a}\right] \quad (5)$$

where ν_0 is the 1D translational zero-point frequency for motion of the particle in the matrix site, a is the width of the barrier, m is the mass of the tunneling particle, and E_a is the barrier height. Equation 5 therefore predicts that the $O(^3P)$ atom diffusion rate should be much smaller than a $H(^2S)$ atom due to the increased mass of the diffusing particle. Indeed, measuring the kinetic isotope effect for a particular process is used to determine the importance of quantum tunneling. For example, the diffusion rate for a D atom on the surface of amorphous water ice is 40 times smaller than a H atom[71] but 100 times smaller on polycrystalline water ice.[72] This difference has been used to argue that the H atom diffusion on amorphous ice is classical and, in contrast, has significant quantum tunneling contributions on polycrystalline water ice.[71−73] However, in this case, they are two different chemical species and tunneling through a square potential also depends on the $O(^3P)$-H_2 and $H(^2S)$-H_2 intermolecular potentials since those will determine the potential parameters (a and E_a) and ν_0, which depend on both the mass of the particle and intermolecular potential parameters.

We show isotropic intermolecular potentials, modeled by Lennard-Jones (12-6) potentials, for both $O(^3P)$-H_2 and

https://doi.org/10.1021/acs.jpca.3c00266
J. Phys. Chem. A 2023, 127, 2751−2764

$H(^2S)$-H_2 in Figure 6a that were taken from the literature.[9,74] Notable from this plot is that while the well depth is 2.6 times

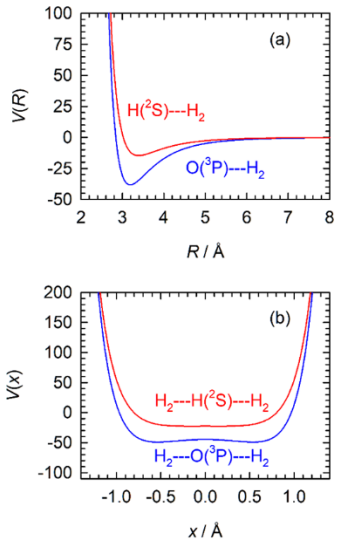

Figure 6. (a) Plot of the LJ (12-6) isotropic potentials (cm^{-1}) as a function of the distance (R) between particles for $H(^2S)$---H_2 and $O(^3P)$---H_2 taken from the literature. Note that while the $O(^3P)$-H_2 potential is significantly deeper, the $O(^3P)$ atom has a smaller hard sphere diameter than $H(^2S)$. (b) Linear p-H_2-X-p-H_2 toy model to estimate the size of a single substitution site for both $O(^3P)$ and $H(^2S)$ calculated with the LJ (12-6) potentials with the distance between p-H_2 molecules fixed at two lattice spacings (7.58 Å). See the text for more details.

deeper for an $O(^3P)$ atom compared to a $H(^2S)$ atom, the $O(^3P)$ atom has a hard sphere diameter of 2.84 Å that is smaller than the $H(^2S)$ atom value of 3.02 Å. The smaller hard sphere diameter for an $O(^3P)$ atom will help reduce the barrier (E_a) to diffusion and could speed up $O(^3P)$ atom quantum diffusion. To give an idea of what the constraining potential looks like for an $O(^3P)$ atom in a single substitutional site in solid p-H_2, we use a simple linear p-H_2-$O(^3P)$-p-H_2 toy model to calculate the 1D potential for translational motion of an $O(^3P)$ atom in between two p-H_2 molecules separated by two lattice spacings (7.58 Å). In the linear toy model, the total potential energy is taken as the sum of the p-H_2-$O(^3P)$ and $O(^3P)$-p-H_2 interactions, i.e., the p-H_2-p-H_2 interaction is ignored. Shown in Figure 6b are the corresponding 1D translational potentials for an $O(^3P)$ atom and $H(^2S)$ atom in solid p-H_2 calculated using the corresponding LJ (12-6) intermolecular potentials shown in Figure 6a. The single substitutional site is bigger for an $O(^3P)$ atom compared to a $H(^2S)$ atom because of the smaller hard sphere diameter for the $O(^3P)$-H_2 intermolecular potential; at $V(x) = 0$ cm^{-1}, the lattice site width is 1.94 Å for an $O(^3P)$ atom and 1.60 Å for a $H(^2S)$ atom. If we model the translational energies for the guest atoms using a particle-in-a-box energy level expression,

$$E_n = \frac{h^2 n^2}{8mL^2} \quad n = 1, 2, \ldots \tag{6}$$

where m is the mass of the particle, and L is the length of the box. We calculate that the 3D zero-point energy for an $O(^3P)$ atom is 8.29 cm^{-1} (2.49×10^9 Hz), while the zero-point energy of a $H(^2S)$ atom is 132 cm^{-1} (3.96×10^{10} Hz). Thus, the ν_0 frequency used in eq 5 is significantly larger for a $H(^2S)$ atom, which should speed up $H(^2S)$ atom diffusion relative to an $O(^3P)$ atom. We can then use eq 5 and the experimentally measured first-order rate constant to estimate the value of E_a if we assume a = 1.0 Å. We predict E_a = 230 cm^{-1} for the $O(^3P)$ atom and E_a = 4360 cm^{-1} for the $H(^2S)$ atom. We interpret this to mean that the $O(^3P)$ atom tunnels over smaller length scales (<1.0 Å) than a $H(^2S)$ atom but that quantum diffusion of an $O(^3P)$ atom can still be facile in solid p-H_2 due primarily to its smaller size. Another significant difference between the two diffusing particles is that the $H(^2S)$ atom is in an s-state, while the $O(^3P)$ atom is in a p-state. Anisotropy in the $O(^3P)$-H_2 interaction may lead to different migration paths through the solid p-H_2 matrix that could also speed up quantum diffusion. In summary, the reaction kinetic measurements presented here demonstrate that $O(^3P)$ atom quantum diffusion in solid p-H_2 is facile even at 1.7 K and is only a factor of two smaller than the diffusion rate for $H(^2S)$ atoms reported in the literature. This likely means that because the O atom is 16 times heavier than a H atom, the potential barriers the $O(^3P)$ atom must tunnel through are smaller, and the tunneling pathlengths are shorter than the corresponding barriers to $H(^2S)$ atom quantum diffusion.

4.2. Comparison with Classical Matrices. It is also instructive to compare the present results for a quantum solid to analogous studies in classical matrices. Kruger and Weitz measured[75] the decay kinetics of $O(^3P)$ atoms formed by photodissociation of N_2O in xenon matrices at temperatures between 30 and 40 K. The most likely decay mechanism in these experiments is diffusion-controlled $O(^3P)$ atom recombination to form O_2. The measured kinetics do not follow a simple second-order rate law as expected for $O(^3P)$ atom recombination, and the authors explain that this is often found for reactions in solids.[75] Yet, they were able to fit the time dependence of the $O(^3P)$ atom by two bimolecular decays and extracted the values 1.4×10^{-15} and 5.4×10^{-18} cm^2 s^{-1} for "fast" and "slow" $O(^3P)$ atom diffusion coefficients at 32 K from fits to the reaction kinetics. The measurements[75] at 40 K produced diffusion coefficients of 7.3×10^{-15} and 2.0×10^{-17} cm^2 s^{-1}, indicating that $O(^3P)$ atom diffusion is thermally activated with an activation energy between 140 and 180 cm^{-1}. This is one of the main differences from the $O(^3P)$ atom reaction studies in solid p-H_2, and the $O(^3P)$ atom quantum diffusion coefficient in solid p-H_2 is nearly independent of temperature over the 1.7 to 4.0 K temperature range. In contrast, in xenon matrices, the $O(^3P)$ atoms can be held almost indefinitely at 10 K and the temperature of the sample must be raised to greater than 30 K to induce $O(^3P)$ atom diffusion at comparable rates.

Another study of the thermal mobility of $O(^3P)$ atoms in a xenon matrix was conducted by Benderskii and Wight in which they studied the effect of crystal morphology on the diffusion-limited geminate recombination of O + O_2 in solid xenon using the 266 nm *in situ* photodissociation of O_3 precursor molecules.[50] They performed photokinetic experiments on both vapor-deposited solids (matrices) and free-standing crystals that showed that the O atom diffusion coefficients extracted for both "slow" and "fast" diffusion is approximately 10 times greater in the free-standing crystals. The free-standing crystals[76] are highly ordered fcc polycrystalline samples with grain sizes on the order of 0.1 mm compared to the vapor-deposited samples (quench condensation) with grain sizes on the order of 100 Å, which are crystalline but strongly disordered, with very small crystallites.[77,78] Thus, like the

https://doi.org/10.1021/acs.jpca.3c00266
J. Phys. Chem. A 2023, 127, 2751−2764

results in solid p-H_2, which showed faster diffusion in annealed samples, the photokinetic experiments in solid xenon show that $O(^3P)$ atom diffusion rates in xenon are faster in crystals with less defects than typical vapor-deposited matrices. They also pointed out that the diffusion coefficients they measured were larger than the ones measured by Kruger and Weitz, which may be related to the different length scales probed in the two experiments; for Benderskii and Wight, the photolysis and recombination occur over length scales of 20 ± 10 Å, while in the experiments of Kruger and Weitz, the length scale is determined by the average distance between O atoms in the matrix produced in the *in situ* photodissociation of N_2O at 193 nm, which varied from 30 Å to greater than 100 Å.[50] The experiments reported here probe length scales more like the experiments of Kruger and Wight since we too use the *in situ* photolysis of O_2 in solid p-H_2 to generate the mobile O atoms, but quantitative estimates of the thermalization length produced in the *in situ* photodissociation of O_2 isolated in solid p-H_2 have not been performed to our knowledge.

Danilychev and Apkarian studied the temperature-induced mobility and recombination of $O(^3P)$ atoms following the *in situ* photolysis of O_2 or N_2O at 193 nm in free-standing crystals of Kr and Xe.[79] By slowly ramping the temperature of the sample while monitoring the "glow curve" produced by O_2 thermoluminescence due to $O(^3P)$ atom recombination, they identified three distinct peaks for Xe solids, which they interpreted as the thermally induced $O(^3P)$ atom diffusion from three distinct matrix sites. The lowest observed peak at 40 K therefore corresponds to $O(^3P)$ atoms trapped in the weakest trapping site for diffusion, while peaks at 47 and 61 K represent more deeply trapped $O(^3P)$ atoms with larger activation energies for migration. Once again, they observed clear differences in the glow curves of O_2 in free-standing crystals and pulse-deposited matrices due to differences in the crystal morphologies. Thermoluminescence measurements at a constant temperature revealed that the thermally induced recombination of trapped $O(^3P)$ atoms in xenon proceeds via first-order kinetics. By modeling the kinetics of thermally activated $O(^3P)$ atom diffusion, they showed that the reason the kinetics is first-order instead of second-order with respect to the $O(^3P)$ atom concentration is due to the long-range migration (~300 Å) of the $O(^3P)$ atoms. This again shows that the kinetic models developed for gas phase reactions can be altered significantly under the conditions of the solid-state environment.

It is also interesting to compare the experimental results in classical matrices with theory. Raff and co-workers[80] employed classical variational transition-state theory to compute diffusion rates and activation energies for diffusion of $O(^3P)$ atoms in fcc argon and xenon crystals. They calculated activation energies for $O(^3P)$ atom diffusion of 0.143 eV (1150 cm^{-1}) and diffusion coefficients $D = 2.48 \times 10^{-23}$ cm^2/s for $O(^3P)$ atoms in xenon at 32 K. The authors therefore concluded that the experimentally observed mobility is predominantly a result of motion along lattice defects, grain boundaries, vacancies, and other lattice imperfections. However, the experimental results that showed faster diffusion in free-standing crystals compared to vapor-deposited matrices indicate that defects slow down diffusion rather than speed it up.

In more recent thermodynamic modeling studies of the thermal migration mechanisms of $O(^3P)$ atoms in noble gas crystals conducted by Buchachenko and co-workers,[81] the calculated barriers were significantly lower (807 cm^{-1}) with activation energies (758 cm^{-1}) only slightly higher than the experimentally determined values. In their paper, Buchachenko and co-workers comment that the earlier theoretical studies of Raff suffered from inaccurate description of the guest−host interaction potential where the anisotropy of the intermolecular interaction between the p-state oxygen atom and host atoms was not considered.[81] Another issue in modeling the solid-state chemistry is that the matrix host must be allowed to relax around the guest species, and the coupling between the guest and the matrix host is very important when calculating the minimum energy pathways to model experiment. Modeling the diffusion in solid p-H_2 requires different theoretical approaches because solid p-H_2 is a quantum solid.

4.3. Comparison with Astronomical Studies. The chemistry that occurs on the surfaces of interstellar dust grains profoundly affects the molecules that are produced in the interstellar medium. At the low temperatures of interstellar dust grains (~10 K), it is well established that surface chemistry proceeds via diffusion of H atoms physisorbed to the surface.[32] What was not known until recently was whether atoms heavier than an H atom could diffuse rapidly enough to react with other species and therefore influence the evolution of molecular complexity in the interstellar medium. In 2013, Minissale *et al.* used O atom bombardment of amorphous solid water (ASW) to study O atom diffusivity and reactivity within the 6−25 K temperature range at submonolayer coverages.[34] In this work, they derived a diffusion temperature law that consisted of quantum tunneling in the lower temperature range (6−22 K) and switched to thermal motion at the higher temperatures (22−25 K). This experiment clearly showed that $O(^3P)$ atom diffusion is faster than previously thought and that $O(^3P)$ atom reactions can become competitive with H atom reactions on the surface of ASW.[34] What remains to be explored further is the balance between classical thermal diffusion (activated hopping) and quantum tunneling under these reaction conditions. This is by no means a solved problem; some have argued[38] that the O atom diffusion rates can be modeled by activated thermal hopping over a distribution of barrier heights, as was used to explain H atom quantum diffusion on water ice.[72] Furthermore, Meuwly and co-workers compared quantum and classical simulations for oxygen atoms diffusing on amorphous ice down to 10 K and showed that tunneling is not required to reproduce the observed diffusion rates.[37] Investigating this balance between classical and quantum diffusion can be accomplished using matrix isolation spectroscopy where classical noble gas matrices allow the $O(^3P)$ atom classical diffusion mechanisms to be studied in detail, while solid p-H_2 is better suited to study $O(^3P)$ atom quantum diffusion and reactivity.

Several of the same conclusions reached in the O atom bombardment work are also found in this study on the quantum diffusion of $O(^3P)$ in bulk solid p-H_2. First, $O(^3P)$ atom diffusion was found to be slightly faster on crystalline water ice surfaces than on amorphous ice, but diffusion on the ASW is still facile. This is consistent with our finding that quantum diffusion of $O(^3P)$ atoms is about a factor of two faster in annealed p-H_2 samples compared to as-deposited samples. This can be rationalized by the idea that the wave packet describing the $O(^3P)$ atom diffuses more quickly on the periodic potential of the crystalline p-H_2 matrix compared to the as-deposited crystal that contains more defects. Second, in a later report,[32] $O(^3P)$ atom diffusion on five different grain surface analogues were studied at low temperature and the

https://doi.org/10.1021/acs.jpca.3c00266
J. Phys. Chem. A 2023, 127, 2751−2764

experimental data were simulated by quantum tunneling through a square barrier. This allows the low-temperature $O(^3P)$ atom diffusion to be fit by two parameters, a and E_a. For three different water surfaces (porous ASW, nonporous ASW, and crystalline water ice), the best fit parameters were a = 0.69−0.70 Å and E_a = 500−530 K, while for annealed p-H_2 samples, we find a = 0.70 and E_a = 680 K. Thus, the tunneling diffusion of $O(^3P)$ atoms on the surface of ASW is comparable to quantum diffusion of $O(^3P)$ atoms in solid p-H_2. Interestingly, the $O(^3P)$ atom diffusion on the surface of ASW at 10 K can be modeled by an Arrhenius formalism with a 300 K thermal diffusion barrier, which is comparable to the 240 ± 80 K thermal diffusion barrier derived from the xenon matrix work of Benderskii and Wight. Thus, the two different types of $O(^3P)$ atom diffusion, thermal hopping and quantum tunneling, can both be studied using classical or quantum matrices, respectively.

5. CONCLUSIONS

Experiments on the 193 nm *in situ* photolysis of O_2 trapped in solid p-H_2 are performed here to measure the diffusion-controlled $O(^3P) + O_2 \rightarrow O_3$ reaction kinetics via FTIR spectroscopy of the O_3 reaction product. Short-term exposure of an O_2-doped p-H_2 solid to 193 nm laser radiation produces small concentrations of $O(^3P)$ atoms than can diffuse through the p-H_2 solid and react with intact O_2 molecules to form O_3. We take special care to irradiate the sample just long enough to generate the needed $O(^3P)$ atoms and therefore minimize the amount of O_3 that gets photolyzed during irradiation, which can lead to the generation of mobile H atoms that could perturb the $O(^3P) + O_2$ reaction kinetics. Thus, in this way, we have optimized the 193 nm photolysis conditions to study the $O(^3P) + O_2$ reaction under pseudo-first-order conditions ($[O_2] > [O]$). The migration of $O(^3P)$ atoms in solid p-H_2 after photolysis is observed via production of O_3 even at temperatures as low as 1.7 K. The O_3 growth curve under these reaction conditions is well fit by a first-order kinetic expression that allows the reaction rate constant to be measured. The rate constant extracted from measurements in annealed p-H_2 crystals at low temperature is more than twice as large as for as-deposited crystals, which contain more lattice defects, showing that $O(^3P)$ atom diffusion is retarded by crystal defects. Experiments conducted at elevated temperatures show that while the reaction rate constant increases slightly, the reaction kinetics are nearly temperature-independent over the 1.7 to 4.0 K temperature range, which is what is expected for $O(^3P)$ atom quantum diffusion. In fact, assuming that the reaction is diffusion-controlled, we can convert the second-order rate constant into a diffusion coefficient by estimating a capture length. The $O(^3P)$ atom diffusion coefficients measured here are almost the same order of magnitude as the $H(^2S)$ atom diffusion coefficients measured previously in solid p-H_2. This was unexpected due to the greater mass of the O atom relative to a H atom where we expected the diffusion rate of $O(^3P)$ atoms to be much slower. Clearly, the $O(^3P)$ atom migration pathway must be different than a $H(^2S)$ atom and yet they diffuse at comparable rates. Furthermore, while $O(^3P)$ atom diffusion in noble gas crystals is thermally activated and thus qualitatively different than quantum diffusion, both diffusion processes are more facile in lattices that have fewer defects. Back in the 1990s, the discrepancy between theory and experiment for the $O(^3P)$ atom diffusion rates in noble gas matrices was attributed to diffusion along lattice defects; however, more recent atomistic simulations have shown that $O(^3P)$ atoms can diffuse on ASW surfaces down to low temperatures (∼10 K) without the requirement of defects.

Another important conclusion from the current studies involves the estimation of the mutual diffusion coefficient D from the second-order reaction rate constant. In general, reactions in solution separate into two limiting cases: diffusion-controlled and activation-controlled. For reactions like $O(^3P) + O_2$, which are essentially barrierless, the assumption is that they follow diffusion-controlled reaction kinetics, which means that the rate constant directly reflects the mutual diffusion coefficient of the reacting pair. However, in solid p-H_2 where the diffusion is governed by quantum tunneling, even though there is no potential barrier along the reaction coordinate for the reaction, the tunneling bandwidth of the $O(^3P)$ atom is much smaller than the energy level mismatch caused by lattice imperfections, and the tunneling rate becomes highly susceptible to perturbations of the matrix potential. As a result, tunneling diffusion slows down significantly at small separations of the reactive pair because of energy mismatches caused by the intermolecular interaction between the two reactive species. The more recent work in H_2 thin films has now firmly established that the diffusion coefficient estimated from H atom recombination kinetics is typically much smaller than the actual diffusion coefficient measured for pure spatial diffusion. This has important ramifications on the interpretation of reaction rate constants that are measured for bimolecular reactions in solid p-H_2 involving mobile impurity atoms such as the $O(^3P)$ atom or $H(^2S)$ atom. Specifically, since each reactive pair will have a different intermolecular potential, some reactions should be slowed down more than the others and, in some cases, quantum diffusion may even lead to no reaction even when the reaction is barrierless in the gas phase.

As discussed previously, diffusion of guest atoms in classical and quantum matrices represents two limiting cases for solid-state diffusion. In classical solids, guest molecules are trapped in matrix sites by potential barriers that can only be overcome by thermal activation. In contrast, guest atom diffusion in quantum matrices such as solid p-H_2 likely involves large contributions from quantum mechanical tunneling but also benefits greatly from the large amount of translational zero-point energy that is inherent to quantum solids. While the detailed $O(^3P)$ diffusion mechanism in solid p-H_2 remains to be characterized, the overlap of the guest atom wavefunction with the nearest neighbor p-H_2 molecules provides an opportunity for the two to exchange places by quantum tunneling. Thus, guest diffusion in quantum solids is not highly dependent on the temperature, and rather $O(^3P)$ atoms in solid p-H_2 keep diffusing even at the lowest temperatures we can achieve experimentally. The $O(^3P) + O_2 \rightarrow O_3$ reaction studies presented here therefore provide direct evidence that $O(^3P)$ atoms quantum-diffuse in solid p-H_2. If the appropriate precursors and reaction conditions can be established, future studies of $O(^3P)$ atoms reactions with different reaction partners could be studied in solid p-H_2 within the 1.7 to 4.3 K temperature range.

■ ASSOCIATED CONTENT

Supporting Information

The Supporting Information is available free of charge at https://pubs.acs.org/doi/10.1021/acs.jpca.3c00266.

https://doi.org/10.1021/acs.jpca.3c00266
J. Phys. Chem. A 2023, 127, 2751−2764

Method used to determine the O_2 concentration, table of integrated absorption coefficients and integration limits used to determine dopant concentrations, table of experimental parameters for the different experiments, table of kinetic parameters determined from least-squares fits of O_3 data to eq 3, representative correlation plot of the para-H_2O concentration measured spectroscopically in the ν_2 and ν_3 regions, all 18 water concentration correlation plots measured in this study, kinetic plots for each experiment on as-deposited samples at low temperatures, low-temperature annealed samples, and annealed samples at elevated temperatures (4.0 K), and temperature and concentration plots for the control experiment (PDF)

AUTHOR INFORMATION

Corresponding Author

David T. Anderson − *Department of Chemistry, University of Wyoming, Laramie, Wyoming 82071, United States;* orcid.org/0000-0002-8959-7661; Email: danderso@uwyo.edu

Authors

Ibrahim Muddasser − *Department of Chemistry, University of Wyoming, Laramie, Wyoming 82071, United States;* orcid.org/0000-0002-1049-8098

Anh H. M. Nguyen − *Department of Chemistry, University of Wyoming, Laramie, Wyoming 82071, United States*

Aaron I. Strom − *Department of Chemistry, University of Wyoming, Laramie, Wyoming 82071, United States*

Aaron M. Hardee − *Department of Chemistry, University of Wyoming, Laramie, Wyoming 82071, United States*

Bryan G. Pluid − *Department of Chemistry, University of Wyoming, Laramie, Wyoming 82071, United States*

Complete contact information is available at: https://pubs.acs.org/10.1021/acs.jpca.3c00266

Notes

The authors declare no competing financial interest.

ACKNOWLEDGMENTS

B.G.P. was supported by the Chemistry NSF REU program (CHE-2051148) hosted at the University of Wyoming. This work was sponsored, in part, by the Chemistry Division of the U.S. National Science Foundation (grant no. CHE-2101719).

REFERENCES

(1) Oka, T. High-resolution spectroscopy of solid hydrogen. *Annu. Rev. Phys. Chem.* **1993**, *44*, 299−333.

(2) Momose, T.; Shida, T. Matrix-isolation spectroscopy using solid parahydrogen as the matrix: Application to high-resolution spectroscopy, photochemistry, and cryochemistry. *Bull. Chem. Soc. Jpn.* **1998**, *71*, 1−15.

(3) Momose, T.; Fushitani, M.; Hoshina, H. Chemical reactions in quantum crystals. *Int. Rev. Phys. Chem.* **2005**, *24*, 533−552.

(4) Yoshioka, K.; Raston, P. L.; Anderson, D. T. Infrared spectroscopy of chemically doped solid parahydrogen. *Int. Rev. Phys. Chem.* **2006**, *25*, 469−496.

(5) Bahou, M.; Huang, C. W.; Huang, Y. L.; Glatthaar, J.; Lee, Y. P. Advances in use of *p*-H_2 as a novel host for matrix IR spectroscopy. *J. Chin. Chem. Soc.* **2010**, *57*, 771−782.

(6) Fajardo, M. E. Matrix isolation spectroscopy in solid parahydrogen. In *Physics and Chemistry at Low Temperaure*; Khriachtchev, L., Ed.; Pan Stanford Publishing: New York, 2011; pp. 167−202.

(7) Bahou, M.; Das, P.; Lee, Y.-F.; Wu, Y.-J.; Lee, Y.-P. Infrared spectra of free radicals and protonated species produced in para-hydrogen matrices. *Phys. Chem. Chem. Phys.* **2013**, *16*, 2200−2210.

(8) Tsuge, M.; Tseng, C. Y.; Lee, Y. P. Spectroscopy of prospective interstellar ions and radicals isolated in para-hydrogen matrices. *Phys. Chem. Chem. Phys.* **2018**, *20*, 5344−5358.

(9) Haupa, K. A.; Joshi, P. R.; Lee, Y. P. Hydrogen-atom tunneling reactions in solid para-hydrogen and their applications to astrochemistry. *J. Chin. Chem. Soc.* **2022**, *69*, 1159−1173.

(10) Andrews, L.; Moskovits, M.: *Chemistry and Physics of Matrix-Isolated Species*; North Holland: Amsterdam, Netherlands, 1989.

(11) Apkarian, V. A.; Schwentner, N. Molecular photodynamics in rare gas solids. *Chem. Rev.* **1999**, *99*, 1481−1514.

(12) Feldman, V. I.; Ryazantsev, S. V.; Kameneva, S. V. Matrix isolation in laboratory astrochemistry: state-of-the-art, implications and perspective. *Russ. Chem. Rev.* **2021**, *90*, 1142−1165.

(13) Hallam, H. E.: *Vibrational Spectroscopy of Trapped Species*; Wiley: New York, 1973.

(14) Moskovits, M. E.; Ozin, G. A.: *Cryochemistry*; Wiley: New York, 1976.

(15) Whittle, E.; Dows, D. A.; Pimentel, G. C. Matrix isolation method for the experimental study of unstable species. *J. Chem. Phys.* **1954**, *22*, 1943−1943.

(16) Nosanow, L. H. Theory of quantum crystals. *Phys. Rev.* **1966**, *146*, 120−133.

(17) Polturak, E.; Gov, N. Inside a quantum solid. *Contemp. Phys.* **2003**, *44*, 145−151.

(18) Silvera, I. F. The solid molecular hydrogens in the condensed phase: Fundamentals and static properties. *Rev. Mod. Phys.* **1980**, *52*, 393−452.

(19) Van Kranendonk, J.: *Solid Hydrogen: Theory of the Properties of Solid H_2, HD, and D_2*; Plenum Press: New York, 1983.

(20) Perutz, R. N. Photochemical reactions involving matrix-isolated atoms. *Chem. Rev.* **1985**, *85*, 77−96.

(21) Miyazaki, T.; Iwata, N.; Lee, K. P.; Fueki, K. Decay of H (D) atoms in solid hydrogen at 4.2 K. Rate constant for tunneling reaction H_2 (D_2, HD) + H (D). *J. Phys. Chem.* **1989**, *93*, 3352−3355.

(22) Ooe, H.; Miyamoto, Y.; Kuma, S.; Kawaguchi, K.; Nakajima, K.; Nakano, I.; Sasao, N.; Tang, J.; Taniguchi, T.; Yoshimura, M. Diffusion of hydrogen fluoride in solid parahydrogen. *J. Chem. Phys.* **2013**, *138*, 6.

(23) Moore, B.; Djuricanin, P.; Momose, T. Diffusion of water molecules in quantum crystals. *J. Phys. Chem. Lett.* **2018**, *9*, 6475−6479.

(24) Okabe, H.: *Photochemistry of Small Molecules*; Wiley: New York, 1978.

(25) Rogers, S.; Wang, D.; Kuppermann, A.; Walch, S. Chemically accurate ab initio potential energy surfaces for the lowest $^3A'$ and $^3A''$ electronically adiabatic states of $O(^3P)$+H_2. *J. Phys. Chem. A* **2000**, *104*, 2308−2325.

(26) Nishida, S.; Taketani, F.; Takahashi, K.; Matsumi, Y. Quantum yield for $O(^1D)$ production from ozone photolysis in the wavelength range of 193-225 nm. *J. Phys. Chem. A* **2004**, *108*, 2710−2714.

(27) Strom, A. I.; Anderson, D. T. Nuclear spin conversion of water confined in solid parahydrogen. *Chem. Phys. Lett.* **2020**, *752*, 137539.

(28) Kufeld, K. A.; Wonderly, W. R.; Paulson, L. O.; Kettwich, S. C.; Anderson, D. T. Transient H_2O infrared satellite peaks produced in UV irradiated formic acid doped solid parahydrogen. *J. Phys. Chem. Lett.* **2012**, *3*, 342−347.

(29) Wonderly, W. R.; Anderson, D. T. Transient HDO rovibrational satellite peaks in solid parahydrogen: Evidence for hydrogen atoms or vacancies? *Low Temp. Phys.* **2012**, *38*, 853−859.

(30) Cuppen, H. M.; Herbst, E. Simulation of the formation and morphology of ice mantles on interstellar grains. *Ap. J.* **2007**, *668*, 294−309.

(31) Tielens, A.; Hagen, W. Model calculations of the molecular composition of interstellar grain mantles. *Astron. Astrophys.* **1982**, *114*, 245−260.

(32) Congiu, E.; Minissale, M.; Baouche, S.; Chaabouni, H.; Moudens, A.; Cazaux, S.; Manico, G.; Pirronello, V.; Dulieu, F. Efficient diffusive mechanisms of O atoms at very low temperatures on surfaces of astrophysical interest. *Faraday Discuss.* **2014**, *168*, 151−166.
(33) Matar, E.; Congiu, E.; Dulieu, F.; Momeni, A.; Lemaire, J. L. Mobility of D atoms on porous amorphous water ice surfaces under interstellar conditions. *Astron. Astrophys.* **2008**, *492*, L17−L20.
(34) Minissale, M.; Congiu, E.; Baouche, S.; Chaabouni, H.; Moudens, A.; Dulieu, F.; Accolla, M.; Cazaux, S.; Manico, G.; Pirronello, V. Quantum tunneling of oxygen atoms on very cold surfaces. *Phys. Rev. Lett.* **2013**, *111*, No. 053201.
(35) Lee, M. W.; Meuwly, M. Diffusion of atomic oxygen relevant to water formation in amorphous interstellar ices. *Faraday Discuss.* **2014**, *168*, 205−222.
(36) Pezzella, M.; Meuwly, M. O_2 formation in cold environments. *Phys. Chem. Chem. Phys.* **2019**, *21*, 6247−6255.
(37) Pezzella, M.; Unke, O. T.; Meuwly, M. Molecular oxygen formation in interstellar ices does not require tunneling. *J. Phys. Chem. Lett.* **2018**, *9*, 1822−1826.
(38) General discussion. *Faraday Discuss.* **2014**, *168*, 129−149, DOI: 10.1039/C4FD90001D.
(39) Fajardo, M. E.; Tam, S. Rapid vapor deposition of millimeters thick optically transparent parahydrogen solids for matrix isolation spectroscopy. *J. Chem. Phys.* **1998**, *108*, 4237−4241.
(40) Tam, S.; Fajardo, M. E. Ortho/Para hydrogen converter for rapid deposition matrix isolation spectroscopy. *Rev. Sci. Instrum.* **1999**, *70*, 1926−1932.
(41) Fajardo, M. E. Solid parahydrogen thickness revisited. *Appl. Spectrosc.* **2019**, *73*, 1403−1408.
(42) Fajardo, M. E. High-resolution rovibrational spectroscopy of carbon monoxide isotopologues isolated in solid parahydrogen. *J. Phys. Chem. A* **2013**, *117*, 13504−13512.
(43) Fajardo, M. E.; Lindsay, C. M. Crystal field splitting of rovibrational transitions of water monomers isolated in solid parahydrogen. *J. Chem. Phys.* **2008**, *128*, No. 014505.
(44) Fajardo, M. E.; Lindsay, C. M.; Momose, T. Crystal field theory analysis of rovibrational spectra of carbon monoxide monomers isolated in solid parahydrogen. *J. Chem. Phys.* **2009**, *130*, 244508.
(45) Fajardo, M. E.; Tam, S.; DeRose, M. E. Matrix isolation spectroscopy of H_2O, D_2O, and HDO in solid parahydrogen. *J. Mol. Struct.* **2004**, *685-696*, 111−127.
(46) Raston, P. L.; Kettwich, S. C.; Anderson, D. T. High-resolution infrared spectroscopy of atomic bromine in solid parahydrogen and orthodeuterium. *J. Chem. Phys.* **2013**, *139*.
(47) Strom, A. I.; Fillmore, K. L.; Anderson, D. T. Hydrogen atom catalyzed ortho-to-para conversion in solid molecular hydrogen. *Low Temp. Phys.* **2019**, *45*, 676−688.
(48) Mutunga, F. M.; Olenyik, K. M.; Strom, A. I.; Anderson, D. T. Hydrogen atom quantum diffusion in solid parahydrogen: The H + N_2O -> cis-HNNO -> trans-HNNO reaction. *J. Chem. Phys.* **2021**, *154*, 16.
(49) Balasubramanian, T. K.; Lien, C.-H.; Rao, K. N.; Gaines, J. R. Observation of the $\Delta J = 4$ pure rotational transitions in solid H_2 and interference of the phonon density of states. *Phys. Rev. Lett.* **1981**, *47*, 1277−1280.
(50) Benderskii, A. V.; Wight, C. A. Diffusion-limited geminate recombination of O+O_2 in solid xenon. *J. Chem. Phys.* **1996**, *104*, 85−94.
(51) Brosset, P.; Dahoo, R.; Gauthier-Roy, B.; Abouaf-Marguin, L.; Lakhlifi, A. Analysis of IR absorption spectrum of O_3 in inert matrices: spectroscopic evidence for two trapping sites. *Chem. Phys.* **1993**, *172*, 315−324.
(52) Lakhlifi, A.; Girardet, C.; Dahoo, R.; Brosset, P.; Gauthier-Roy, B.; Abouaf-Marguin, L. Interpretation of the infrared spectrum of ozone trapped in inert matrices. *Chem. Phys.* **1993**, *177*, 31−44.
(53) Moore, B.; Bashiri, T.; Otani, H.; Djuricanin, P.; Malekfar, R.; Farahbod, A. H.; Momose, T. VUV photochemistry and nuclear spin conversion of water and water-orthohydrogen complexes in para-hydrogen crystals at 4 K. *Phys. Chem. Chem. Phys.* **2021**, *23*, 4094−4106.
(54) Bakker, B. L. G.; Parker, D. H. Photophysics of O_2 excited by tunable laser radiation around 193 nm. *J. Chem. Phys.* **2000**, *112*, 4037−4044.
(55) Danilychev, A. V.; Apkarian, V. A. Photo-stationary state of UV pumped matrix-isolated O_2. *Chem. Phys. Lett.* **1995**, *246*, 139−144.
(56) Danilychev, A. V.; Bondybey, V. E.; Apkarian, V. A.; Tanaka, S.; Kajihara, H.; Koda, S. Photodynamics in oxygen doped solid deuterium. *J. Chem. Phys.* **1995**, *103*, 4292−4299.
(57) Babikov, D.; Kendrick, B. K.; Walker, R. B.; Pack, R. T.; Fleurat-Lesard, P.; Schinke, R. Metastable states of ozone calculated on an accurate potential energy surface. *J. Chem. Phys.* **2003**, *118*, 6298−6308.
(58) Babikov, D.; Kendrick, B. K.; Walker, R. B.; Schinke, R.; Pack, R. T. Quantum origin of an anomalous isotope effect in ozone formation. *Chem. Phys. Lett.* **2003**, *372*, 686−691.
(59) Andreev, A. F.; Lifshitz, I. M. Quantum theory of defects in crystals. *Soviet Physics JETP-USSR* **1969**, *29*, 1107−1107.
(60) Guyer, R. A.; Zane, L. I. Tunneling and exchange in quantum solids. *Phys. Rev.* **1969**, *188*, 445−468.
(61) Oyarzun, R.; Van Kranendonk, J. Quantum diffusion in solid hydrogen and deuterium. *Phys. Rev. Lett.* **1971**, *26*, 646−648.
(62) Oyarzun, R.; Van Kranendonk, J. Theory of quantum diffusion in solid hydrogen and deuterium. I. Calculation of the jump frequency. *Can. J. Phys.* **1972**, *50*, 1494−1510.
(63) Andreev, A. F. Diffusion in quantum crystals. *Uspekhi Fiz. Nauk* **1976**, *118*, 251−271.
(64) Meyerovich, A. E. Quantum diffusion and pairing of ortho-H_2 impurities in para-H_2. *Phys. Rev. B* **1990**, *42*, 6068−6075.
(65) Kumada, T. Experimental determination of the mechanism of the tunneling diffusion of H atoms in solid hydrogen: Physical exchange versus chemical reaction. *Phys. Rev. B* **2003**, *68*, No. 052301.
(66) Kumada, T.; Sakakibara, M.; Nagasaka, T.; Fukuta, H.; Kumagai, J.; Miyazaki, T. Absence of recombination of neighboring H atoms in highly purified solid parahydrogen: Electron spin resonance, electron-nuclear double resonance, and electron spin echo studies. *J. Chem. Phys.* **2002**, *116*, 1109−1119.
(67) Raston, P. L.; Anderson, D. T. Infrared-induced reaction of Cl atoms trapped in solid parahydrogen. *Phys. Chem. Chem. Phys.* **2006**, *8*, 3124−3129.
(68) Raston, P. L.; Kettwich, S. C.; Anderson, D. T. Kinetic studies of the infrared-induced reaction between atomic chlorine and solid parahydrogen. *J. Mol. Spectrosc.* **2015**, *310*, 72−83.
(69) Sheludiakov, S.; Lee, D. M.; Khmelenko, V. V.; Dmitriev, Y. A.; Jarvinen, J.; Ahokas, J.; Vasiliev, S. Purely spatial diffusion of H atoms in solid normal- and para-hydrogen films. *Phys. Rev. B* **2022**, *105*, 144102.
(70) Sheludiakov, S.; Lee, D. M.; Khmelenko, V. V.; Jarvinen, J.; Ahokas, J.; Vasiliev, S. Purely spatial quantum diffusion of H atoms in solid H_2 at temperatures below 1 K. *Phys. Rev. Lett.* **2021**, *126*, 195301.
(71) Hama, T.; Kuwahata, K.; Watanabe, N.; Kouchi, A.; Kimura, Y.; Chigai, T.; Pirronello, V. The mechanism of surface diffusion of H and D atoms on amorphous solid water: Existence of various potential sites. *Ap. J.* **2012**, *757*, 1−12.
(72) Kuwahata, K.; Hama, T.; Kouchi, A.; Watanabe, N. Signatures of quantum-tunneling diffusion of hydrogen atoms on water ice at 10 K. *Phys. Rev. Lett.* **2015**, *115*, 133201.
(73) Hama, T.; Watanabe, N. Surface processes on interstellar amorphous solid water: Adsorption, diffusion, tunneling Reactions, and nuclear-spin conversion. *Chem. Rev.* **2013**, *113*, 8783−8839.
(74) Dagdigian, P. J.; Kłos, J.; Warehime, M.; Alexander, M. H. Accurate transport properties for O(^{3}P)-H and O(^{3}P)-H_2. *J. Chem. Phys.* **2016**, *145*, 164309.
(75) Krueger, H.; Weitz, E. O(^{3}P) atom lifetimes and mobilities in xenon matrices. *J. Chem. Phys.* **1992**, *96*, 2846−2855.

(76) Rudnick, W.; Haensel, R.; Nahme, H.; Schwentner, N. Luminescence efficiency and grain sizes of Ar crystals. *Phys. Status Solidi A* **1985**, *87*, 319−322.
(77) Steinmetz, N.; Menges, H.; Dutzi, J.; Löhneysen, H. V.; Goldacker, W. Specific heat of disordered Xe films at low temperatures. *Phys. Rev. B* **1989**, *39*, 2838−2841.
(78) Menges, H.; Löhneysen, H. V. Specific heat of disordered and amorphous rare-gas solids: Quench-condensed pure and binary films. *J. Low Temp. Phys.* **1991**, *84*, 237−260.
(79) Danilychev, A. V.; Apkarian, V. A. Temperature induced mobility and recombination of atomic oxygen in crystalline Kr and Xe. I. Experiment. *J. Chem. Phys.* **1993**, *99*, 8617−8627.
(80) Ford, M. B.; Foxworthy, A. D.; Mains, G. J.; Raff, L. M. Theoretical investigations of O_3 vibrational-relaxation and oxygen-atom diffusion rates in Ar and Xe matrices. *J. Phys. Chem.* **1993**, *97*, 12134−12143.
(81) Leibin, I. V.; Kalinina, I. S.; Bezrukov, D. S.; Buchachenko, A. A. Modeling of the thermal migration mechanisms of atomic oxygen in Ar, Kr, and Xe crystals. *J. Chem. Phys.* **2021**, *154*, No. 044305.

https://doi.org/10.1021/acs.jpca.3c00266
J. Phys. Chem. A 2023, 127, 2751−2764